telecom

MDPI

Article

Toward Green 6G Networks: NOMA-Based Reconfigurable Intelligent Surfaces with Hybrid Acoustic–Magnetic Energy Harvesting

Ghaffer Iqbal Kiani

Department of Electrical and Computer Engineering, King Abdulaziz University, Jeddah 21589, Saudi Arabia; gkiani@kau.edu.sa

Abstract

This work introduces a novel self-sustainable wireless communication architecture that combines RIS and NOMA with a hybrid acoustic–magnetic energy harvesting framework. The source node operates under strict energy constraints and is powered by harvesting ambient acoustic vibrations and surrounding magnetic fields, enabling autonomous transmission to multiple NOMA users. To enhance propagation conditions, an RIS is deployed to intelligently control the wireless channel by optimizing its phase response, thereby strengthening desired signals and suppressing interference.The performance of the proposed system is analytically characterized under the hybrid energy harvesting model. The derived expressions provide insight into the interaction between harvested energy dynamics, RIS configuration, and NOMA transmission. Simulation results confirm that the proposed RIS-NOMA architecture significantly outperforms conventional orthogonal and non-orthogonal access schemes in both spectral and energy efficiency. In addition, the hybrid harvesting mechanism ensures more stable energy availability, improving reliability in highly energy-constrained environments.

Keywords: RIS; NOMA; acoustic energy harvesting; magnetic energy harvesting; energy-efficient wireless communications

1. Introduction

The proliferation of connected devices in next-generation wireless networks has intensified the need for communication systems that can operate with minimal or no external power supply. This requirement is particularly critical in scenarios such as industrial monitoring, underwater sensing, and remote IoT deployments, where replacing or recharging batteries is impractical.

Among the various EH sources, acoustic and magnetic energy harvesting have received increasing attention due to their suitability in harsh or infrastructure-limited environments. Acoustic energy, typically generated from mechanical vibrations or sound waves, is abundant in industrial machinery and underwater environments. In contrast, magnetic energy harvesting exploits ambient electromagnetic fields or inductive coupling effects commonly found near power lines and electrical equipment. By combining these two sources, hybrid acoustic–magnetic harvesting offers improved robustness against energy fluctuations and environmental variability.

At the same time, advanced communication technologies such as RIS and NOMA have become key components of 6G and beyond networks. RIS technology enables programmable control of wireless propagation by intelligently adjusting the electromagnetic

Check for updates

Academic Editor: Achilles Boursianis

Received: 6 July 2026
Revised: 18 August 2026
Accepted: 25 August 2026
Published: 10 September 2026

Copyright: © 2026 by the author. Licensee MDPI, Basel, Switzerland. This article is an open access article distributed under the terms and conditions of the Creative Commons Attribution (CC BY) license.

response of surface elements, leading to improved coverage and reduced fading effects. Meanwhile, NOMA improves spectral efficiency by allowing multiple users to share the same resource block through power-domain multiplexing.

Motivated by these developments, this paper studies an RIS-assisted NOMA system powered by hybrid acoustic–magnetic energy harvesting at the transmitter. The RIS is configured to enhance the effective channel gain for multiple users, while the transmitter adapts its communication strategy based on the available harvested energy.

The main contributions of this work are as follows:

- A unified framework integrating RIS, NOMA, and hybrid acoustic–magnetic energy harvesting is developed.
- Analytical expressions for throughput and energy efficiency are derived under realistic channel and harvesting conditions.
- A joint design approach for RIS phase optimization and NOMA power allocation is proposed.
- Results demonstrate the superiority of the system over conventional baseline schemes. Although RIS-assisted NOMA systems have been extensively investigated, most existing works assume conventional energy supplies or RF energy harvesting models. These assumptions do not capture the stochastic characteristics of alternative ambient energy sources such as acoustic vibrations and magnetic fields. This work develops a unified communication framework that explicitly models hybrid acoustic–magnetic harvested energy and integrates it with RIS-assisted NOMA transmission. The proposed framework jointly considers energy randomness, RIS phase optimization, NOMA power allocation, outage probability, BLER, and throughput optimization.

Energy harvesting has recently attracted significant attention as an enabling technology for self-sustainable wireless networks, particularly for applications where battery replacement is difficult or impossible. Acoustic energy harvesting has been investigated for underwater communication, structural monitoring, and low-power sensing applications. Khan et al. provided a comprehensive survey of energy harvesting techniques in underwater acoustic wireless sensor networks, highlighting the challenges associated with energy availability, conversion efficiency, and sustainable operation [1]. Several works have focused on improving acoustic-to-electric conversion efficiency through advanced transducer and circuit designs. Wang et al. proposed an active rectifier with adaptive delay control and frequency detection techniques to enhance the efficiency of acoustic wave energy harvesting systems [2]. Similarly, piezoelectric and triboelectric acoustic harvesting approaches have been investigated to improve energy extraction from low-frequency environmental vibrations. In particular, Tsuchiya et al. explored acoustic energy harvesting using mechanical–acoustic coupling mechanisms [3], while Yu et al. introduced a Helmholtz resonator-based triboelectric nanogenerator for enhanced acoustic energy conversion [4]. Recent studies have also considered acoustic harvesting in communication systems. For example, Mittal et al. investigated energy harvesting in NOMA-based UAV acoustic networks, demonstrating the potential of harvested acoustic energy for supporting wireless transmission [5].

Magnetic field energy harvesting has also received considerable interest due to the availability of electromagnetic sources in industrial environments, power transmission systems, and transportation infrastructures. Xu et al. studied the optimization of magnetic field energy harvesters for power-line applications and analyzed techniques for improving harvested energy efficiency [6]. Xiao et al. proposed a transfer-window modulation strategy and power management approach to improve the performance of magnetic energy harvesting systems [7]. Several researchers have focused on improving the conversion efficiency through advanced circuit interfaces, impedance matching, and power man-

agement techniques. Dillersberger et al. developed a low-voltage AC/DC conversion interface with impedance matching for magnetic field energy harvesting applications [8], while Mahato et al. proposed an efficient synchronous magnetic flux extraction circuit to improve energy utilization [9]. Moreover, Gao et al. investigated core desaturation and switching-based approaches to maximize magnetic energy extraction under varying operating conditions [10–13].

Magnetic harvesting has also been applied in practical sensing and monitoring systems. Tao et al. analyzed magnetic energy harvesting solutions for freight train sensor applications [14], while Zhao et al. developed a lightweight self-powered module for remote sensing in transmission lines [15]. Similarly, Wu et al. investigated magnetic-field-powered sensing systems for high-voltage converter monitoring [16]. Other studies have explored broadband and vibration-assisted magnetic harvesting techniques to improve energy availability under dynamic environmental conditions [17–19]. In addition, hybrid electromagnetic–mechanical harvesting approaches have been proposed to enhance the harvested power by combining multiple conversion mechanisms [20].

Although significant progress has been achieved in improving acoustic and magnetic energy harvesting hardware, most existing works focus primarily on circuit design, transducer optimization, or harvested power improvement. The integration of stochastic energy harvesting models with advanced wireless communication techniques remains relatively unexplored. Existing RIS-assisted NOMA systems generally assume conventional battery-powered transmitters or deterministic energy sources and do not consider the statistical characteristics of ambient acoustic and magnetic energy sources. Furthermore, limited attention has been given to the joint optimization of harvested energy, RIS phase configuration, and NOMA transmission performance. Motivated by this research gap, this work develops a unified analytical framework that integrates hybrid acoustic–magnetic energy harvesting with RIS-assisted NOMA communication, where the stochastic harvested energy directly influences the available transmission power and system throughput.

Although energy harvesting, RIS, and NOMA technologies have been extensively investigated individually, their joint integration has only recently attracted attention. Existing energy harvesting studies mainly focus on improving energy conversion efficiency, power management, and hardware implementation, while RIS research primarily aims at controlling wireless propagation through programmable electromagnetic surfaces. The combination of RIS and energy harvesting provides a promising solution for future self-sustainable communication networks, where harvested energy can support the operation of low-power devices and RIS can compensate for the severe propagation losses experienced in energy-constrained scenarios. Recent works on RIS-assisted wireless powered communication have demonstrated that intelligent reflecting surfaces can improve energy transfer efficiency and communication reliability by enhancing the effective channel gain. However, most existing RIS-enabled energy harvesting frameworks consider RF-based energy harvesting with deterministic or simplified energy models and do not capture the stochastic characteristics of ambient energy sources such as acoustic and magnetic fields.

Furthermore, RIS-assisted NOMA systems have shown significant potential for improving spectral efficiency by enabling simultaneous transmission to multiple users through intelligent channel control and power-domain multiplexing. However, current RIS-NOMA investigations generally assume conventional battery-powered transmitters or dedicated RF energy sources, neglecting the impact of random harvested energy availability on resource allocation and transmission performance. On the other hand, existing acoustic and magnetic energy harvesting studies mainly evaluate harvested power improvement without considering communication-level metrics such as outage probability, throughput, or block error rate. Therefore, a gap remains in developing a unified analytical framework

that integrates multi-source ambient energy harvesting with RIS-assisted NOMA transmission. The proposed work addresses this gap by jointly considering stochastic hybrid acoustic–magnetic energy generation, RIS phase optimization, and NOMA communication performance within a single framework.

2. Review

Harvesting has become a fundamental enabler for autonomous wireless networks, allowing communication devices to operate using ambient energy sources. This is particularly the case in applications involving industrial monitoring and power infrastructure environments. Prior studies have explored different magnetic harvesting architectures aimed at improving energy conversion efficiency and power regulation. For instance, Xu et al. and Xiao et al. developed optimization strategies for magnetic harvesting systems based on transfer window control and phase management techniques. Similarly, Liu et al. analyzed harmonic magnetic field extraction for powering sensors deployed in high-voltage transmission systems.

Significant efforts have also been directed toward improving hardware design and circuit-level efficiency in magnetic energy harvesting systems. Several researchers have proposed advanced core structures, voltage control mechanisms, and energy storage interfaces to enhance harvested power stability. Works in this area have further extended to include supercapacitor integration and synchronous rectification techniques to improve energy utilization efficiency. In addition, magnetic harvesting has been successfully applied in measurement systems, resonant devices, and wireless sensing applications.

In parallel, acoustic energy harvesting has emerged as an alternative energy solution, particularly suitable for underwater communication systems and structural health monitoring. Research in this domain has focused on improving acoustic-to-electric conversion efficiency through resonant structures, metamaterials, and triboelectric nanogenerators. Recent developments include adaptive rectification circuits and engineered acoustic structures designed to enhance broadband energy capture.

To further improve energy availability, hybrid harvesting systems combining multiple sources such as acoustic, magnetic, and mechanical vibrations have been proposed. These multi-modal approaches demonstrate improved energy stability and higher overall power output compared to single-source harvesters. Additionally, coupling mechanisms and metamaterial-based designs have been introduced to enhance energy conversion efficiency across different frequency ranges.

Recent studies have also investigated the integration of energy harvesting with NOMA-based systems, particularly in UAV and IoT scenarios, highlighting improved energy utilization and system performance.

More recently, Reconfigurable Intelligent Surfaces (RISs) have been combined with advanced multiple access schemes to enhance wireless coverage and spectral efficiency. However, despite these advancements, limited research has addressed the joint integration of RIS-assisted NOMA systems with hybrid acoustic–magnetic energy harvesting. This work aims a unified framework combining these emerging technologies for improved energy efficiency and communication performance.

Li et al. [21] developed a pixel-controlled programmable metasurface for phase-type spatial terahertz modulation, demonstrating that intelligent control of metasurface elements can significantly improve electromagnetic wave manipulation. Although their work focuses on terahertz modulation, it further illustrates the potential of programmable metasurfaces as a key enabling technology for RIS-assisted wireless communications, motivating their integration with advanced multiple access and energy harvesting techniques. Luo [22] discussed the emerging concept of digital optics and optical intelligent agents, highlighting

how programmable optical platforms and artificial intelligence can jointly enable adaptive electromagnetic wave manipulation. This vision further emphasizes the increasing role of intelligent programmable surfaces in future 6G communication systems and motivates the development of RIS-assisted wireless architectures with enhanced adaptability and energy efficiency.

Although considerable research has been devoted independently to energy harvesting, Reconfigurable Intelligent Surfaces (RISs), and non-orthogonal multiple access (NOMA), only a limited number of studies investigate their joint integration. Existing RIS-assisted NOMA systems primarily assume conventional battery-powered transmitters or RF energy harvesting and therefore neglect the stochastic characteristics of alternative ambient energy sources. Consequently, the interaction between harvested energy dynamics and RIS-assisted wireless transmission remains insufficiently understood.

Similarly, previous studies on magnetic energy harvesting mainly focus on improving harvester efficiency through optimized coil structures, resonance tuning, impedance matching, power management circuits, and magnetic flux enhancement techniques. These investigations primarily address hardware implementation issues and rarely consider communication-level performance metrics such as outage probability, block error rate (BLER), or achievable throughput in wireless communication systems. Likewise, recent research on acoustic energy harvesting has concentrated on piezoelectric transducers, triboelectric nanogenerators, acoustic metamaterials, Helmholtz resonators, and broadband resonant structures for maximizing harvested power. Although these studies significantly improve energy conversion efficiency, they generally do not integrate harvested acoustic energy into modern RIS-assisted wireless communication frameworks.

Hybrid energy harvesting has recently emerged as an effective solution for improving the reliability of self-powered wireless devices by exploiting multiple ambient energy sources. Existing hybrid harvesting architectures typically combine solar, radio-frequency, vibration, thermal, or wind energy. However, the combination of acoustic and magnetic energy harvesting has received very limited attention despite the complementary characteristics of these two ambient energy sources in industrial environments, power transmission systems, railway infrastructures, and underwater sensing applications. Furthermore, existing hybrid harvesting studies usually evaluate harvested power or hardware efficiency without establishing analytical communication models capable of characterizing transmission reliability.

Recent investigations have also explored the integration of energy harvesting with NOMA and RIS technologies. Nevertheless, these works generally optimize either RIS beamforming or communication resource allocation while assuming conventional energy supply models. To the best of our knowledge, no previous work has simultaneously developed a unified analytical framework incorporating hybrid acoustic–magnetic energy harvesting, RIS-assisted NOMA transmission, outage probability analysis, BLER analysis, harvesting-time optimization, and throughput optimization within the same mathematical model.

Motivated by these observations, this paper develops a unified communication-theoretic framework that explicitly models the stochastic harvested energy obtained from acoustic and magnetic ambient sources. The harvested energy directly determines the available transmission power of the NOMA source, while the RIS intelligently adjusts the propagation environment through phase alignment to maximize the equivalent cascaded channel gain. In addition, harvesting duration is jointly optimized with RIS-assisted transmission to maximize the achievable throughput. This integrated analytical framework distinguishes the proposed work from existing RIS-assisted energy harvesting studies,

which generally investigate these technologies independently rather than within a unified mathematical formulation.

3. Energy Acquisition via Acoustic Waves

The amount of power recoverable from sound-based sources is modeled as

$$\mathcal{P}_{\text{acoustic}} = \mathcal{I}_s \cdot \xi \cdot \mathcal{A} \tag{1}$$

with the parameters defined as

- $\mathcal{P}_{\text{acoustic}}$: Acoustic power captured (in Watts);
- $\mathcal{I}_s$: Acoustic power density (W/m^2);
- ξ: Efficiency factor of the conversion device;
- $\mathcal{A}$: Effective capture surface.

The sound intensity $\mathcal{I}_s$ relates to the root mean square acoustic pressure ψ as

$$\mathcal{I}_s = \frac{\psi^2}{\varrho v} \tag{2}$$

where

- ψ: Sound pressure amplitude (Pa);
- ϱ: Medium's mass density (kg/m^3);
- v: Speed of sound in the propagation medium (m/s).

By substitution, we obtain

$$\mathcal{P}_{\text{acoustic}} = \xi \cdot \left(\frac{\psi^2}{\varrho v}\right) \cdot \mathcal{A} \tag{3}$$

4. Acoustic Pressure Statistical Profile

The pressure amplitude ψ is assumed to follow a normal distribution:

$$\psi \sim \mathcal{N}(\mu_\psi, \sigma_\psi^2) \tag{4}$$

The energy collected over a time window of duration αT, where $0 < \alpha < 1$, is given by

$$\mathcal{E}_{\text{acoustic}} = \alpha T \cdot \mathcal{P}_{\text{acoustic}} \tag{5}$$

If T_s is the symbol duration, the energy per symbol becomes

$$\mathcal{E}_{\text{sym}}^{acoustic} = \frac{\mathcal{E}_{\text{acoustic}}}{\frac{(1-\alpha)T}{T_s}} = \frac{\alpha T_s \mathcal{P}_{\text{sound}}}{1-\alpha} = \kappa \cdot \psi^2 \tag{6}$$

with the constant defined as

$$\kappa = \frac{\alpha T_s}{1-\alpha} \cdot \left(\frac{\xi \mathcal{A}}{\varrho v}\right) \tag{7}$$

Given the Gaussian nature of ψ, the variable $\mathcal{E}_{\text{sym}}$ follows a scaled non-central chi-squared distribution. Its probability density function is expressed as [23]

$$f_{\mathcal{E}_{\text{sym}}^{acoustic}}(x) = \frac{0.5}{\kappa\sigma_\psi^2} \exp\left[-\frac{1}{2}\left(\frac{x}{\kappa\sigma_\psi^2} + \frac{\mu_\psi^2}{\sigma_\psi^2}\right)\right]\left(\frac{x}{\kappa\mu_\psi^2}\right)^{-0.25}$$
$$\times I_{-0.5}\left(\frac{\mu_\psi}{\sigma_\psi^2}\sqrt{\frac{x}{\kappa}}\right) \tag{8}$$

The acoustic and magnetic harvested energies are obtained by scaling the square of Gaussian random variables. Therefore, the resulting distributions follow scaled non-central chi-square distributions with one degree of freedom.

5. Magnetic-Based Energy Collection

Let us consider a coil-based harvester subjected to a time-varying magnetic field. If the coil consists of $\mathcal{N}$ turns and each loop has area $\mathcal{S}$, and the magnetic density varies as $\mathcal{B}(t)$, the magnetic flux threading the coil is

$$\Phi(t) = \mathcal{B}(t) \cdot \mathcal{S} = B_{\text{peak}} \mathcal{S} \cos(2\pi f_m t) \tag{9}$$

where

- B_{peak}: Maximum field strength (in Teslas);
- f_m: Field oscillation frequency (Hz);
- $\mathcal{S}$: Effective surface per turn (m^2).

5.1. Voltage Generation via Electromagnetic Induction

According to Faraday's law, the electromotive force (EMF) across the coil is

$$\mathcal{V}_{\text{ind}}(t) = -\mathcal{N} \cdot \frac{d\Phi(t)}{dt} = 2\pi f_m \mathcal{N} B_{\text{peak}} \mathcal{S} \sin(2\pi f_m t) \tag{10}$$

5.2. Instantaneous and Mean Power Delivered

If the coil feeds a purely resistive load of resistance R_L, the instantaneous power transfer is

$$P_{\text{inst}}(t) = \frac{\mathcal{V}_{\text{ind}}(t)^2}{R_L} = \frac{(2\pi f_m \mathcal{N} B_{\text{peak}} \mathcal{S})^2 \sin^2(2\pi f_m t)}{R_L} \tag{11}$$

Averaging over one cycle, noting $\langle \sin^2(2\pi f_m t) \rangle = 0.5$, the mean harvested power becomes

$$\overline{P}_{\text{mag}} = \frac{\mathcal{N}^2 (2\pi f_m)^2 B_{\text{peak}}^2 \mathcal{S}^2}{2R_L} \tag{12}$$

This result can also be reformulated for clarity:

$$\overline{P}_{\text{mag}} = \frac{2\pi^2 \mathcal{N}^2 f_m^2 B_{\text{peak}}^2 \mathcal{S}^2}{R_L} \tag{13}$$

Key observations:

- Greater B_{peak} increases induced voltage.
- Larger coil area $\mathcal{S}$ leads to higher flux.
- Higher frequency f_m enhances output, assuming system resonance is matched.
- The load resistance R_L influences power extraction efficiency.

5.3. Random Frequency Model for Ambient Fields

In practical scenarios, the excitation frequency f_m may not be fixed. When ambient sources like electrical appliances, motors, or wireless transmissions overlap, their cumulative effect can lead to frequency variations. Based on the Central Limit Theorem, we assume that f_m follows a Gaussian distribution:

$$f_m \sim \mathcal{N}(\mu_f, \sigma_f^2) \tag{14}$$

5.4. Harvested Energy and Symbol-Level Energy

The energy captured over a duration αT is

$$\mathcal{E}_{\text{mag}} = \alpha T \cdot \overline{P}_{\text{mag}} \tag{15}$$

Given symbol duration T_s, the energy allocated per symbol becomes

$$\mathcal{E}_{\text{sym}}^{\text{mag}} = \frac{\alpha T_s}{1-\alpha} \cdot \overline{P}_{\text{mag}} = \lambda \cdot f_m^2 \tag{16}$$

where

$$\lambda = \frac{2\pi^2 B_{\text{peak}}^2 \mathcal{N}^2 \mathcal{S}^2 \alpha T_s}{(1-\alpha) R_L} \tag{17}$$

Assuming $f_m \sim \mathcal{N}(\mu_f, \sigma_f^2)$, then $\mathcal{E}_{\text{sym}}^{\text{mag}} = \lambda f_m^2$ also follows a non-central chi-square distribution, and its PDF is given by

$$f_{\mathcal{E}_{\text{sym}}^{magnetic}}(y) = \frac{0.5}{\lambda \sigma_f^2} \exp\left[-\frac{1}{2}\left(\frac{y}{\lambda \sigma_f^2} + \frac{\mu_f^2}{\sigma_f^2}\right)\right] \left(\frac{y}{\lambda \mu_f^2}\right)^{-0.25} \times I_{-0.5}\left(\frac{\mu_f}{\sigma_f^2}\sqrt{\frac{y}{\lambda}}\right) \tag{18}$$

The proposed energy harvesting model is intended for communication-level performance analysis rather than detailed circuit design. Practical acoustic and magnetic energy harvesters include several nonlinear phenomena, including resonance bandwidth limitations, impedance matching networks, rectifier nonlinearities, magnetic core saturation, storage capacitor dynamics, leakage losses, and power management circuitry. Explicitly modeling each of these mechanisms would considerably increase the analytical complexity and obscure the communication-theoretic insights developed in this work. Therefore, following a common approach adopted in analytical energy harvesting communication models, these hardware-dependent effects are represented through the overall energy conversion efficiencies ξ and the corresponding harvesting coefficients. Consequently, the proposed model should be interpreted as a first-order statistical abstraction suitable for evaluating wireless communication performance rather than as a detailed electrical model of practical harvesting hardware.

The acoustic pressure amplitude is assumed to follow a Gaussian distribution,

$$\psi \sim \mathcal{N}(\mu_\psi, \sigma_\psi^2),$$

which is motivated by the Central Limit Theorem. In many industrial environments, the received acoustic field is generated by the superposition of numerous independent sound and vibration sources. Under these conditions, the aggregate pressure fluctuations can be accurately approximated by a Gaussian random process over the observation interval considered. Since the harvested acoustic power is proportional to the acoustic intensity, which itself is proportional to the squared pressure amplitude, the harvested acoustic energy naturally follows a scaled non-central chi-square distribution.

Similarly, the magnetic harvester is excited by ambient time-varying magnetic fields generated by surrounding electrical equipment. Although practical electromagnetic sources often exhibit dominant periodic components, their effective excitation frequency may fluctuate because of multiple simultaneously operating devices, harmonic components, switching converters, rotating machinery, and environmental disturbances. Therefore, the equivalent excitation frequency is modeled as a Gaussian random variable around its

nominal operating value, providing a tractable statistical representation for communication performance analysis. Under this assumption, the harvested magnetic energy is also modeled as a scaled non-central chi-square random variable.

Throughout this work, the acoustic and magnetic harvesting processes are assumed to be statistically independent because they originate from distinct physical mechanisms and generally arise from unrelated environmental phenomena. Consequently, the total harvested energy is expressed as

$$E_{\mathrm{H}} = E_{\mathrm{A}} + E_{\mathrm{M}},$$

and its probability density function is obtained through the convolution

$$f_{E_{\mathrm{H}}}(x) = f_{E_{\mathrm{A}}}(x) * f_{E_{\mathrm{M}}}(x).$$

Although this assumption is appropriate for many practical industrial environments, extending the proposed framework to correlated harvesting sources constitutes an interesting direction for future research.

5.5. Table of Typical Parameters

Table 1 shows typical parameters for electromagnetic energy harvesting.

Table 1. Simulation parameters for electromagnetic energy harvesting using updated notation.

Symbol	Typical Value	Unit
$\mathcal{N}$	100	—
f_m	10	Hz
B_{peak}	0.01	T
$\mathcal{S}$	0.01	m^2
R_L	100	Ω

5.6. Hybrid Magnetic and Acoustic Energy Harvesting

The total harvested energy from acoustic signals and magnetic field is equal to

$$\mathcal{E}_{sym} = \mathcal{E}_{sym}^{magnetic} + \mathcal{E}_{sym}^{acoustic} \tag{19}$$

The PDF of E_s is equal to

$$f_{\mathcal{E}_{sym}}(y) = f_{\mathcal{E}_{sym}^{magnetic}} * f_{\mathcal{E}_{sym}^{acoustic}}(y) \tag{20}$$

If the acoustic and magnetic harvesting processes are statistically correlated, the convolution expression is no longer valid. Let ρ denote the correlation coefficient between the harvested acoustic energy E_{A} and the harvested magnetic energy E_{M}. In this case, the probability density function of the total harvested energy must be obtained from the joint probability density function as

$$f_{E_{\mathrm{H}}}(x) = \int_0^x f_{E_{\mathrm{A}},E_{\mathrm{M}}}(y, x-y)\, dy, \tag{21}$$

where $f_{E_{\mathrm{A}},E_{\mathrm{M}}}(x,y)$ denotes the joint probability density function of the acoustic and magnetic harvested energies. Therefore, the convolution in [20] is a special case corresponding to statistically independent harvesting processes.

6. RIS Using NOMA Performance Analysis

The system model with K NOMA users using RIS is shown in Figure 1.

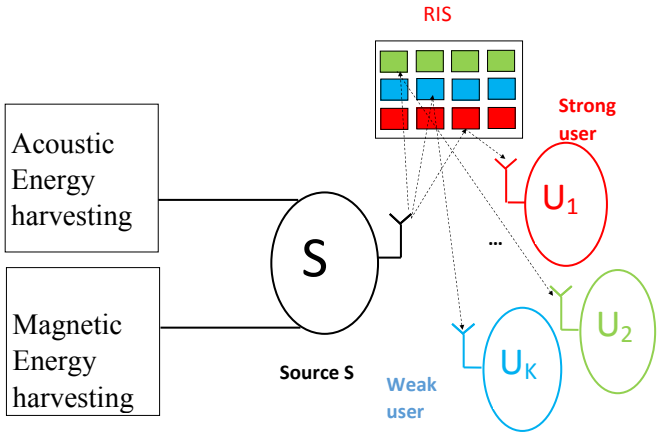


Figure 1. Magnetic and acoustic energy harvesting using NOMA and RIS for 6G.

The broadcasted NOMA symbol is expressed as

$$s = \sqrt{E_s} \sum_{i=1}^{K} \sqrt{p_i} s_i, \tag{22}$$

where s_i is the symbol of U_i, $p_K > p_{K-1} > ... > p_1 > 0$, $\sum_{i=1}^{K} p_i = 1$.

We define $\sqrt{\lambda_1} h_k$ the channel from S to the k-th IS element, $h_k = a_k e^{-j\theta_k}$ and $\sqrt{\lambda_2} g_{k,i}$ as the channel from k-th IS element to U_i with $g_{k,i} = b_{k,i} e^{-j\psi_{k,i}}$.

The phase of RIS is

$$\Phi_{k,i} = \theta_k + \psi_{k,i}. \tag{23}$$

U_i signal is

$$y_i = s\sqrt{E_s \lambda_1 \lambda_2} \sum_{k \in J_i} h_k g_{k,i} e^{j\Phi_{k,i}} + n_i, \tag{24}$$

where J_i is IS elements dedicated to U_i and n_i is a random term due to noise.

We deduce

$$y_i = s\sqrt{E_s \lambda_1 \lambda_2} A_i + n_i, \tag{25}$$

where

$$A_i = \sum_{k \in J_i} a_k b_{k,i} \tag{26}$$

The SINR at U_i is

$$\Gamma_{i \to K} = \frac{Y_i p_K}{N_0 + Y_i \sum_{n=1}^{K-1} p_n} \tag{27}$$

where

$$Y_i = E_s A_i^2 \lambda_1 \lambda_2. \tag{28}$$

The SINR at U_i is

$$\Gamma_{i \to j} = \frac{Y_i p_j}{N_0 + Y_i \sum_{n=1}^{j-1} p_n}. \tag{29}$$

N_0 represents the additive white Gaussian noise power at the receiver. The adopted outage and BLER analytical procedures follow the methodology presented in the Proakis Book [23].

U_i outage probability is given by

$$P_{outage,i} = F_{Y_i}(\max_{i \le l \le K}(\frac{N_0 x}{p_l - x\sum_{n=1}^{l-1} p_n})) \tag{30}$$

The block error rate (BLER) at U_i is

$$BLER_i(\alpha) < P_{outage,i}(W) \tag{31}$$

where the waterfall threshold is given in [24] and written as

$$W = \int_0^{+\infty} 1 - [1 - (1 - \frac{1}{\sqrt{m}})Q(\sqrt{\frac{3v}{m-1}})]^L dv, \tag{32}$$

m is constellation size and L is packet length.

The throughput of U_i is

$$Thr_i(\alpha) = [1 - BLER_i(\alpha)](1 - \alpha)log_2(M). \tag{33}$$

The total throughput is

$$Thr(\alpha) = \sum_{i=1}^{K} Thr_i(\alpha). \tag{34}$$

$Thr(\alpha)$ is maximized using

$$Thr_{max} = \max_{0<\alpha<1} Thr(\alpha). \tag{35}$$

6.1. Y_i CDF

The CDF of A_i^2 is [24]

$$F_{A_i^2}(x) \simeq \frac{1}{2} erfc\left(\frac{-m_{A_i} - \sqrt{x}}{\sqrt{2}\sigma_{A_i}}\right) - \frac{1}{2} erfc\left(\frac{-m_{A_i} + \sqrt{x}}{\sqrt{2}\sigma_{A_i}}\right) \tag{36}$$

where $m_{A_i} = E(A_i) = \frac{N_i \pi}{4}$, $\sigma_{A_i}^2 = Var(A_i) = N_i(1 - \frac{\pi^2}{16})$.

We deduce

$$F_{Y_i}(x) = \int f_{E_s}(y) F_{A_i^2}(\frac{x}{y\lambda_1\lambda_2}) dy. \tag{37}$$

6.2. RIS-NOMA System Model and Optimization Framework

The considered system consists of one energy-constrained source node S, an RIS equipped with N reflecting elements, and K NOMA users denoted by U_i, $i = 1, \ldots, K$. The source node is powered by the hybrid acoustic–magnetic energy harvesting mechanism described previously. The harvested energy during the harvesting duration αT is stored and subsequently used for NOMA transmission during the remaining interval $(1 - \alpha)T$.

The RIS is divided into K independent partitions, where each partition contains a subset of reflecting elements dedicated to one user. Let J_i denote the set of RIS elements assigned to user U_i, where

$$\bigcup_{i=1}^{K} J_i = \{1, 2, \ldots, N\}, \tag{38}$$

and

$$J_i \cap J_j = \emptyset, \quad i \neq j. \tag{39}$$

The partition size is denoted by $N_i = |J_i|$, and therefore

$$\sum_{i=1}^{K} N_i = N. \tag{40}$$

This partitioning strategy enables the RIS to simultaneously support multiple NOMA users by allocating independent phase-control groups.

6.3. Channel Model and Path Loss

The channel between the source node and the k-th RIS element is expressed as

$$h_k = \sqrt{\lambda_1} a_k e^{-j\theta_k}, \tag{41}$$

where λ_1 represents the corresponding path-loss coefficient and a_k follows a Nakagami-m or Rayleigh fading amplitude distribution. Similarly, the channel between the k-th RIS element and user U_i is given by

$$g_{k,i} = \sqrt{\lambda_2} b_{k,i} e^{-j\psi_{k,i}}, \tag{42}$$

where λ_2 denotes the RIS-user path-loss coefficient.

The path-loss coefficients are modeled as

$$\lambda_1 = d_{SR}^{-\eta_1}, \tag{43}$$

and

$$\lambda_2 = d_{RU_i}^{-\eta_2}, \tag{44}$$

where d_{SR} and d_{RU_i} represent the corresponding distances and η_1 and η_2 are the path-loss exponents.

6.4. RIS Phase Design

The RIS phase matrix is defined as

$$\mathbf{\Theta} = diag(e^{j\Phi_{1,i}}, ..., e^{j\Phi_{N,i}}). \tag{45}$$

For user U_i, the optimal phase compensation aligns the reflected signals from all RIS elements belonging to J_i. Therefore, the phase shift of the k-th reflecting element is selected as

$$\Phi_{k,i} = \theta_k + \psi_{k,i}, \quad k \in J_i. \tag{46}$$

With this design, all reflected components add constructively and the equivalent RIS channel becomes

$$A_i = \sum_{k \in J_i} a_k b_{k,i}. \tag{47}$$

Consequently, the received signal power coefficient is

$$Y_i = E_s A_i^2 \lambda_1 \lambda_2. \tag{48}$$

6.5. NOMA User Ordering and SIC Model

The users are ordered according to their effective channel gains as

$$Y_1 \leq Y_2 \leq ... \leq Y_K. \tag{49}$$

Following the conventional power-domain NOMA principle, more power is allocated to users with weaker channel conditions. Hence, the power coefficients satisfy

$$p_1 \geq p_2 \geq ... \geq p_K, \tag{50}$$

with

$$\sum_{i=1}^{K} p_i = 1. \tag{51}$$

The transmitted NOMA signal is

$$s = \sqrt{E_s} \sum_{i=1}^{K} \sqrt{p_i} s_i. \tag{52}$$

User U_i applies successive interference cancellation (SIC) by decoding signals of weaker users before detecting its own message. The SINR for decoding user U_j at user U_i is

$$\Gamma_{i \to j} = \frac{\Upsilon_i p_j}{N_0 + \Upsilon_i \sum_{n=1}^{j-1} p_n}. \tag{53}$$

For imperfect SIC, a residual interference factor ζ can be introduced as

$$\Gamma_{i \to j}^{I} = \frac{\Upsilon_i p_j}{N_0 + \zeta \Upsilon_i \sum_{n=1}^{j-1} p_n + \Upsilon_i \sum_{n=j+1}^{K} p_n}, \tag{54}$$

where $\zeta = 0$ represents perfect SIC and $0 < \zeta < 1$ represents imperfect interference cancellation.

6.6. Joint RIS Partition, Phase and Power Optimization

The joint optimization problem is formulated to maximize the system throughput:

$$\max_{\alpha, \mathbf{p}, \mathbf{\Phi}} \sum_{i=1}^{K} Thr_i(\alpha) \tag{55}$$

subject to

$$0 < \alpha < 1, \tag{56}$$

$$\sum_{i=1}^{K} p_i = 1, \tag{57}$$

$$p_i \geq 0, \tag{58}$$

and

$$|\Phi_{k,i}| \leq 2\pi. \tag{59}$$

The optimization is solved using an alternating optimization approach. First, the RIS phases are optimized according to channel phase compensation. Then, the NOMA power coefficients are optimized while keeping the RIS configuration fixed. Finally, the harvesting duration α is updated to maximize the throughput–energy tradeoff.

The proposed optimization has polynomial complexity. The RIS phase design requires $\mathcal{O}(N)$ operations, while the power allocation optimization requires $\mathcal{O}(K)$ iterations. Therefore, the overall complexity is approximately

$$\mathcal{O}(N + K). \tag{60}$$

This framework provides a practical low-complexity solution for RIS-assisted NOMA transmission powered by stochastic hybrid acoustic–magnetic energy harvesting.

7. Results

This section presents the simulation results for the proposed Reconfigurable Intelligent Surface (RIS)-assisted system employing magnetic and acoustic energy harvesting. The performance is analyzed in terms of system throughput under different RIS sizes and energy harvesting configurations. The effects of the number of reflecting elements N, hybrid energy harvesting, and harvesting duration α are examined.

It is important to distinguish between the simulation scenarios considered in Figures 1–7. In Figures 1–4, the harvesting duration is fixed at $\alpha = 0.5$, meaning that half of the transmission frame is allocated to energy harvesting while the remaining half is used for information transmission. Since the achievable throughput is proportional to the effective transmission time $(1 - \alpha)$, the maximum normalized throughput is naturally limited to approximately 1 bit/s/Hz under this fixed operating point. In contrast, Figures 5–7 employ the optimal harvesting duration obtained from the optimization problem

$$\alpha^{\star} = \arg \max_{0<\alpha<1} \mathrm{Thr}(\alpha),$$

which jointly balances the harvested energy and the available transmission interval. The optimized value of α provides a higher transmit power while preserving sufficient communication time, allowing the throughput to approach its theoretical maximum of approximately 2 bit/s/Hz for the adopted modulation and system configuration. This explains the different throughput saturation levels observed in the simulation figures.

To ensure reproducibility, all simulation parameters used in this work are summarized in Table 1. The wireless channels between the source, RIS, and users follow independent Rayleigh fading with large-scale path loss determined by the adopted propagation model. Unless otherwise stated, all numerical results are obtained by averaging over 10^6 independent Monte Carlo channel realizations to ensure statistical accuracy and convergence of the simulated performance metrics.

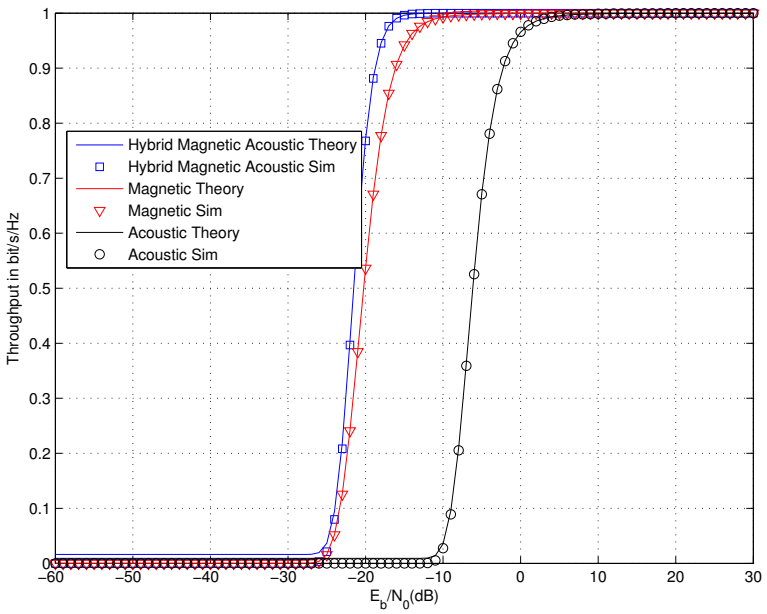


Figure 2. Throughput for magnetic and acoustic energy harvesting for $N = 8$.

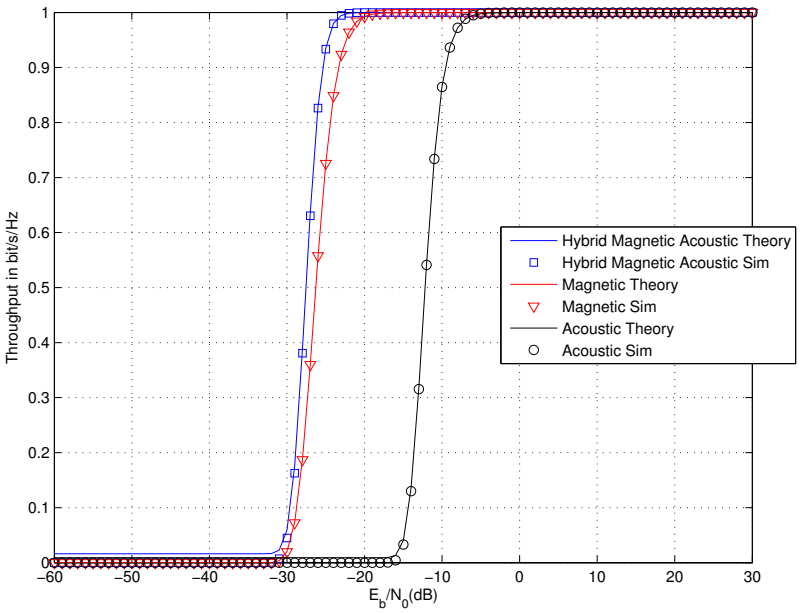


Figure 3. Throughput for magnetic and acoustic energy harvesting for $N = 16$.

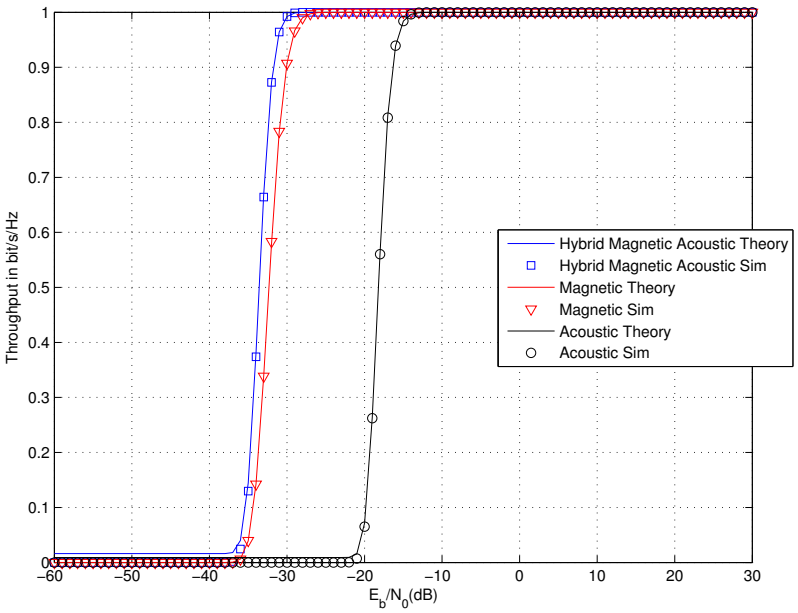


Figure 4. Throughput for magnetic and acoustic energy harvesting for $N = 32$.

To further quantify the agreement between the analytical expressions and the Monte Carlo simulation results, the root-mean-square error (RMSE) is employed as an accuracy metric. The RMSE between the theoretical throughput values and the simulated data points is calculated as

$$\text{RMSE} = \sqrt{\frac{1}{M}\sum_{m=1}^{M}\left(T_{\text{th}}(m) - T_{\text{sim}}(m)\right)^2}, \tag{61}$$

where M denotes the number of simulation points, $T_{\text{th}}(m)$ represents the theoretical throughput obtained from the derived analytical model, and $T_{\text{sim}}(m)$ is the corresponding Monte Carlo simulation result. The obtained RMSE values for all considered scenarios are very small, confirming the high accuracy of the proposed analytical framework. This close agreement between theoretical and simulation results validates the correctness of the derived expressions and demonstrates that the proposed model can accurately char-

acterize the performance of the RIS-assisted hybrid magnetic–acoustic energy harvesting NOMA system.

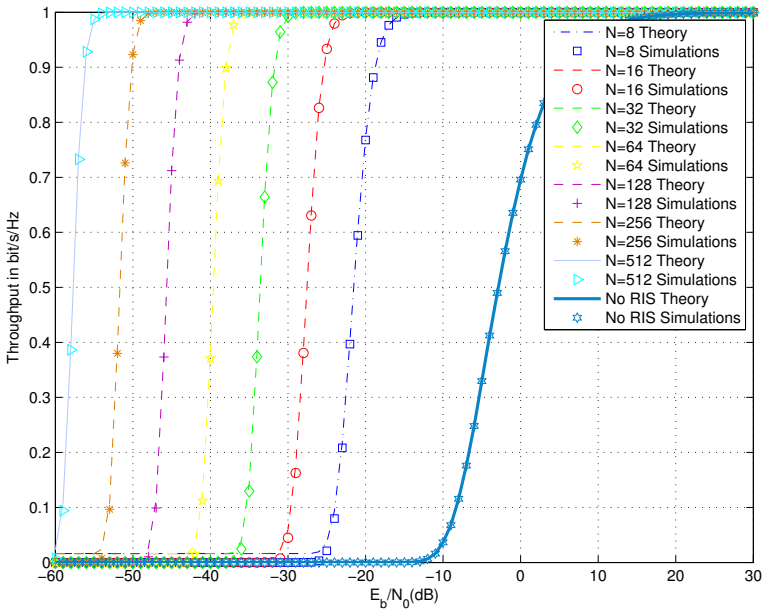


Figure 5. Throughput for hybrid magnetic and acoustic energy harvesting for N = 8, 16, 32, 64, 128, 256, 512 compared to non-RIS.

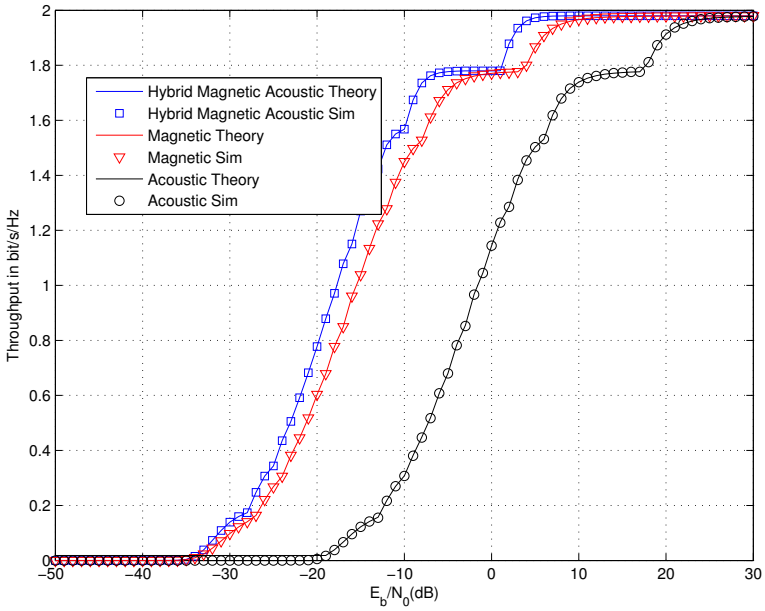


Figure 6. Throughput for magnetic and acoustic energy harvesting for $N = 8$ under optimal harvesting duration α.

The RMSE values obtained using 10^6 Monte Carlo realizations are below 1.5×10^{-3} bit/s/Hz for all considered scenarios, confirming the excellent agreement between the analytical derivations and simulation results.

The wireless propagation channels are modeled using a distance-dependent large-scale path-loss model with a path-loss exponent of $\eta = 3$, representing a typical urban wireless environment. The thermal noise power spectral density is set to -174 dBm/Hz. Unless otherwise stated, quadrature phase-shift keying (QPSK) modulation is adopted, corresponding to a modulation order of $M = 4$. The packet length is fixed to L = 10,000 symbols for the

BLER and throughput evaluations. The NOMA power allocation coefficients are optimized and satisfy $\sum_{i=1}^{K} p_i = 1$ with $p_1 > p_2 > \cdots > p_K$, ensuring that users with weaker channel conditions receive higher transmission power in accordance with the NOMA principle. All simulation results are obtained by averaging over 10^6 independent Monte Carlo channel realizations to ensure statistically reliable performance estimates.

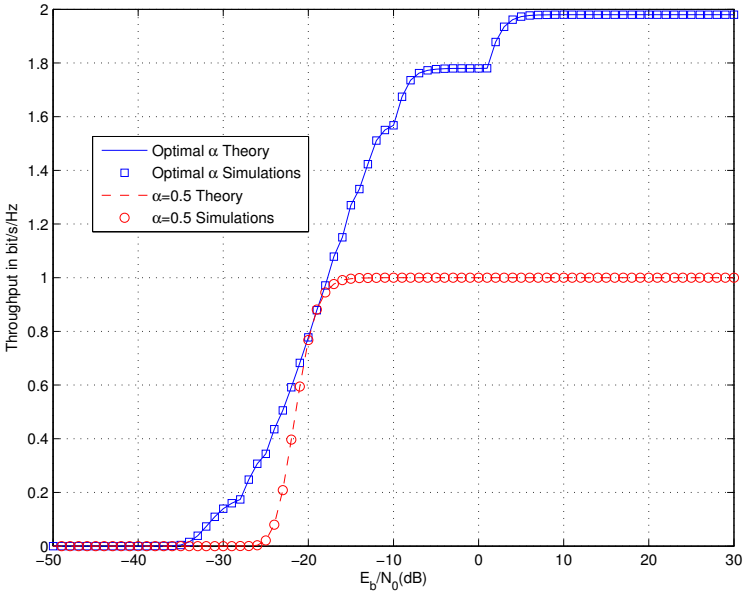


Figure 7. Throughput for hybrid magnetic and acoustic energy harvesting for $N = 8$ at $\alpha = 0.5$ and optimized α.

In all figures, the parameter $\frac{E_b}{N_0}$ represents the average signal-to-noise ratio (SNR) per bit, where E_b denotes the transmitted energy per bit and N_0 represents the noise power spectral density.

7.1. Throughput Performance for Different RIS Sizes

Figures 2–4 illustrate the throughput of the system for magnetic and acoustic energy harvesting when the number of reflecting elements is varied as $N = 8$, $N = 16$, and $N = 32$, respectively. As observed in Figure 2, for $N = 8$, the throughput increases with signal-to-noise ratio (SNR), indicating that stronger harvested energy results in improved data transmission capability. However, since the RIS array is relatively small, the performance gain is limited.

When the number of RIS elements increases to $N = 16$, as shown in Figure 3, a significant improvement in throughput is achieved. The larger RIS provides greater control over phase alignment, which enhances signal reflection and constructive interference at the receiver.

Figure 4 demonstrates the performance for $N = 32$. The results confirm that increasing the number of RIS elements further boosts throughput and energy utilization efficiency. This scalability shows the potential of RIS-assisted systems to significantly enhance wireless performance as array size grows.

7.2. Impact of Hybrid Energy Harvesting

Figure 5 compares the throughput of the proposed hybrid magnetic–acoustic energy harvesting system with that of a conventional non-RIS setup for different RIS sizes ($N = 8$, 16, 32, 64, 128, 256, 512). The throughput increases monotonically with N, demonstrating the strong influence of RIS beamforming on system performance. The hybrid energy harvesting

configuration consistently outperforms both magnetic-only and acoustic-only schemes, highlighting the advantage of combining multiple ambient energy sources.

7.3. Effect of Harvesting Duration Optimization

In Figure 6, the throughput performance for magnetic and acoustic energy harvesting with $N = 8$ is shown under optimal α. As α increases, more time is allocated for energy harvesting, but less remains for data transmission. The curve reveals an optimal value of α that maximizes throughput.

Figure 7 compares hybrid magnetic–acoustic harvesting performance for $N = 8$ at fixed $\alpha = 0.5$ and at the optimized value of α. The optimized configuration achieves higher throughput at medium-to-high SNRs, confirming the efficiency of adaptive time allocation.

Figure 8 shows the throughput variation versus α for different average SNR values (0, -10, and -20 dB) when $N = 8$. The throughput first increases with α, reaches a peak, and then decreases due to reduced data transmission time. The optimal harvesting duration slightly shifts with SNR, showing that the best α depends on the available signal power. At higher SNR levels, the system achieves notably higher maximum throughput.

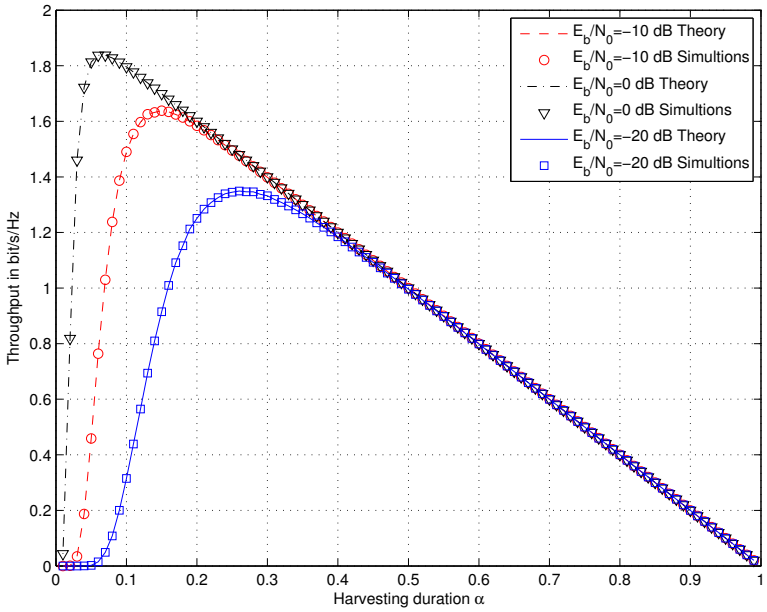


Figure 8. Throughput of hybrid magnetic-and-acoustic energy harvesting versus harvesting duration α for different average SNR values and $N = 8$.

7.4. Discussion

The simulation results confirm that increasing the number of RIS elements significantly enhances system throughput due to improved channel gain aggregation and phase alignment. The hybrid energy harvesting model effectively utilizes both magnetic and acoustic sources, providing a stable and renewable energy supply. Moreover, optimizing the harvesting duration α yields substantial gains in system efficiency by balancing energy intake and transmission time. These results validate the feasibility of RIS-assisted hybrid energy harvesting as a sustainable solution for future wireless networks.

Figure 9 compares the throughput performance of non-orthogonal multiple access (NOMA) and orthogonal multiple access (OMA) in a hybrid magnetic–acoustic energy harvesting system assisted by a Reconfigurable Intelligent Surface (RIS) with eight reflecting elements. The results show that NOMA achieves higher throughput than OMA in the medium- and high-SNR regimes, whereas OMA outperforms NOMA at low SNR due to

inter-user interference in the NOMA scheme. The performance evaluation considers two NOMA users and employs Quadrature Phase Shift Keying (QPSK) modulation.

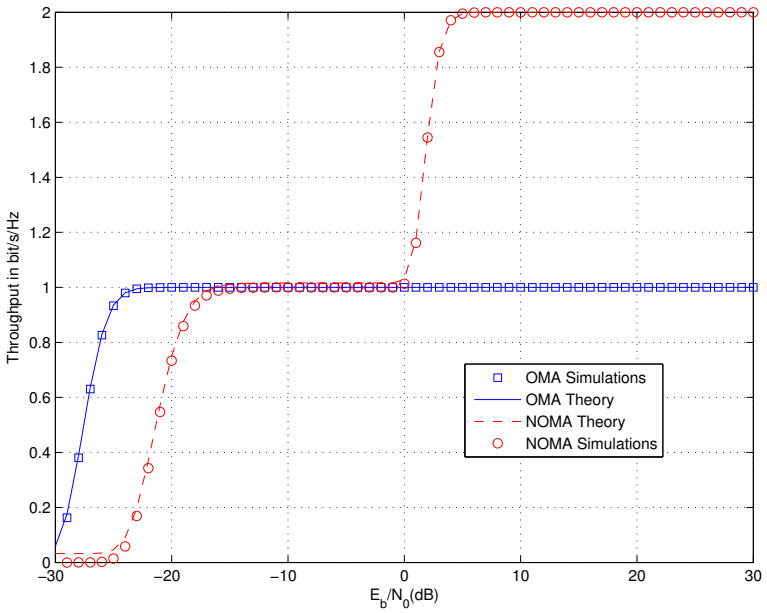


Figure 9. Throughput of hybrid magnetic and acoustic energy harvesting using NOMA or OMA and RIS for $N = 8$.

8. Conclusions

This paper introduced a 6G system powered by hybrid acoustic-and-magnetic energy harvesting at the source node. The hybrid EH model ensures reliable and continuous power availability by jointly harvesting energy from ambient magnetic and acoustic fields. The RIS effectively enhances the wireless channel by intelligently reflecting signals toward the NOMA users, thereby improving both energy and spectral efficiency. Analytical and numerical results demonstrate that the proposed system outperforms conventional NOMA and OMA systems, particularly in energy-limited or signal-blocked environments.

The proposed framework provides several advantages, including improved propagation conditions through RIS phase optimization, enhanced spectral efficiency through NOMA transmission, and improved energy availability through hybrid acoustic–magnetic harvesting. However, practical implementation faces challenges related to nonlinear harvesting circuits, imperfect channel state information, and optimization complexity. Future research will investigate low-complexity optimization methods, imperfect SIC, and practical energy storage models for large-scale 6G deployments.

In this work, an ideal RIS phase compensation model is adopted to characterize the performance gains of the proposed RIS-assisted hybrid magnetic–acoustic energy harvesting NOMA system. However, practical RIS implementations may introduce additional non-ideal effects, such as reflection amplitude losses, phase-dependent attenuation, and inter-element crosstalk between adjacent reflecting elements. These factors may slightly degrade the achievable throughput compared with the idealized model. Since the main objective of this work is to analyze the fundamental performance benefits of RIS-assisted energy harvesting and NOMA integration, these effects are assumed to be negligible. As a future research direction, a more practical RIS model considering hardware impairments, amplitude–phase coupling, manufacturing imperfections, and mutual coupling between RIS elements will be investigated to further evaluate the robustness of the proposed framework under realistic deployment conditions.

Funding: This project was funded by the Deanship of Scientific Research (DSR) at King Abdulaziz University, Jeddah, Saudi Arabia, under Grant no. (IPP:550-135-2025). The author, therefore, acknowledges with thanks DSR for technical and financial support.

Data Availability Statement: The original contributions presented in this study are included in the article. Further inquiries can be directed to the corresponding author.

Conflicts of Interest: The author declares no conflicts of interest.

Abbreviations

The following abbreviations are used in this manuscript:

6G	Sixth-Generation Wireless Communications
RIS	Reconfigurable Intelligent Surface
NOMA	Non-Orthogonal Multiple Access
OMA	Orthogonal Multiple Access
EH	Energy Harvesting
SIC	Successive Interference Cancellation
IoT	Internet of Things
UAV	Unmanned Aerial Vehicle
SNR	Signal-to-Noise Ratio
SINR	Signal-to-Interference-plus-Noise Ratio
PDF	Probability Density Function
CDF	Cumulative Distribution Function
BLER	Block Error Rate
BER	Bit Error Rate
QoS	Quality of Service
CSI	Channel State Information
LOS	Line-of-Sight
NLOS	Non-Line-of-Sight
MC	Monte Carlo
QPSK	Quadrature Phase Shift Keying
EMF	Electromotive Force
RF	Radio Frequency

References

1. Khan, A.; Imran, M.; Alharbi, A.; Mohamed, E.M.; Fouda, M.M. Energy Harvesting in Underwater Acoustic Wireless Sensor Networks: Design, Taxonomy, Applications, Challenges and Future Directions. *IEEE Access* **2022**, *10*, 82463–82490. [CrossRef]
2. Wang, B.; Miao, W.; Kaiquan, B.; Ma, X. A 20–20 kHz Active Rectifier with Adaptive Delay Time Control and 1000X Frequency Detecting Techniques for Acoustic Wave Energy Harvesting. In Proceedings of the 2021 IEEE International Conference on Integrated Circuits, Technologies and Applications (ICTA), Zhuhai, China, 24–26 November 2021.
3. Tsuchiya, M.; Tsuchiya, H.; Moriyama, H.; Uchida, H.T.; Nagasaka, S.; Suzuki, Y. The Energy Harvesting System by Using Internal Acoustic Energy at Both Side Excitation. In Proceedings of the ACTUATOR 2022; International Conference and Exhibition on New Actuator Systems and Applications, Mannheim, Germany, 29–30 June 2022.
4. Yu, H.; Du, T.; Zhao, H.; Zhang, Q.; Liu, L.; Mtui, A.E.; Huang, Y.; Xiao, X.; Xu, M. Conical Helmholtz Resonator-Based Triboelectric Nanogenerator for Harvesting of Acoustic Energy. In Proceedings of the IEEE 16th International Conference on Nano/Micro Engineered and Molecular Systems (NEMS), Xiamen, China, 25–29 April 2021.
5. Mittal, K.; Gupta, A.; Garg, P. Energy Harvesting in NOMA based UAV-Acoustic system. In Proceedings of the IEEE 20th India Council International Conference (INDICON), Telangana, India, 14–17 December 2023.
6. Xu, C.; Wang, W.; Shi, Y.; Su, W.; Hu, M. Comparative Analysis and Optimization of Magnetic Field Energy Harvesters Based on Split Three-Phase Power Line Joint Energy Harvesting. *IEEE Trans. Ind. Inform.* **2025**, *21*, 4617–4627. [CrossRef]
7. Xiao, H.; Peng, H.; Zhao, Y.; Hou, L. Magnetic Field Energy Harvesting and Power Management With Transfer Window Modulation. *IEEE Trans. Power Electron.* **2025**, *40*, 7573–7585. [CrossRef]

8. Dillersberger, H.; Tham, D.; Deutschmann, B. A Sub-100 mV AC/DC Converter with Impedance Matching for Magnetic Field Energy Harvesting. In Proceedings of the 18th Conference on Ph.D Research in Microelectronics and Electronics (PRIME), Valencia, Spain, 18–21 June 2023.
9. Mahato, M.; Sen, S.; Mukherjee, B. An Efficient Synchronous Magnetic Flux Extraction Interface with Auxiliary Circuit for Electromagnetic Energy Harvesting. In Proceedings of the IEEE 21st India Council International Conference (INDICON), Kharagpur, India, 19–21 December 2024.
10. Gao, M.; Yi, L.; Moon, J. Intracycle Gapless Core Desaturation via Crisscross Switches for Maximal Magnetic Energy Harvesting. *IEEE Trans. Ind. Electron.* **2025**, *72*, 2476–2486. [CrossRef]
11. Gao, M.; Moon, J. Core Desaturation via Crisscross Switches for Maximal Magnetic Energy Harvesting. In Proceedings of the 2024 IEEE Energy Conversion Congress and Exposition (ECCE), Phoenix, AZ, USA, 20–24 October 2024.
12. Gao, M.; Yi, L.; Moon, J. Improving Magnetic Energy Harvesting via Desaturation with Reverse Voltage. In Proceedings of the IEEE Applied Power Electronics Conference and Exposition (APEC), Long Beach, CA, USA, 25–29 February 2024.
13. Gao, M.; Yi, L.; Moon, J. Enabling Multiple Harvesting Windows in Magnetic Energy Harvesting via Reverse Flux Desaturation. *IEEE J. Emerg. Sel. Top. Power Electron.* **2024**, *12*, 2517–2530. [CrossRef]
14. Tao, J.; Wang, Y.; Cheng, H.; Mai, R. Analysis and Design of Magnetic Field Energy Harvesting for Freight Train Sensors. *IEEE Trans. Transp. Electrif.* **2024**, *10*, 4503–4512. [CrossRef]
15. Zhao, Y.; Peng, H.; Xiao, H.; Hou, L.; Yan, Y.; Chen, W.; Li, C. A Lightweight Self-Powered Module Based on Magnetic Energy Harvesting for Transmission Line Remotely Sensing. In Proceedings of the IEEE 10th International Power Electronics and Motion Control Conference (IPEMC2024-ECCE Asia), Chengdu, China, 17–20 May 2024.
16. Wu, Y.; Xia, Y.; Ma, S.; Zhu, Z.; Chen, Y. Temperature and Voltage Measurements for High Voltage Converter Testing Bench Based on Magnetic Field Energy Harvesting Sensor. In Proceedings of the IEEE China International Youth Conference on Electrical Engineering (CIYCEE), Wuhan, China, 6–8 November 2024.
17. Li, L.; Xiao, H.; Peng, H.; Ao, C.; Du, J.; Sun, H. Magnetic Field Energy Harvesting with Broad Frequency Band. In Proceedings of the IEEE 6th International Electrical and Energy Conference (CIEEC), Hefei, China, 12–14 May 2023.
18. Yanase, T.; Yoshida, Y.; Hiraga, M.; Miura, N. A Magnetic Softening Resonator With Flat Power Generation for Nonlinear Vibration Energy Harvesting. In Proceedings of the IEEE 23rd International Conference on Micro and Miniature Power Systems, Self-Powered Sensors and Energy Autonomous Devices (PowerMEMS), Tonsberg, Norway, 18–21 November 2024.
19. Okada, T.; Fujieda, S.; Seino, S.; Nakagawa, T. Evaluation of Magnetic Flux Density Change for Vibration Energy Harvesting: Comparison Between Direct and Indirect Measurements. *IEEE Trans. Magn.* **2023**, *59*, 2501205. [CrossRef]
20. Gao, X.; Cui, J.; Zheng, Y.; Li, G. An Electromagnetic-Piezoelectric Hybrid Harvester Based on Magnetic Circuit Switch for Vibration Energy Harvesting. *IEEE Access* **2023**, *11*, 65075–65083. [CrossRef]
21. Li, G.; Li, G.; He, Z.; Wang, X.; Klar, P.J.; Ma, H.; Zhang, Y. Pixel-controlled programmable metasurface as phase-type spatial terahertz modulator. *Opto-Electron. Adv.* **2026**, *9*, 260028. [CrossRef]
22. Luo, X. Digital optics and optical intelligent agent. *Appl. Phys. Lett.* **2025**, *127*, 010501. [CrossRef]
23. Proakis, J. *Digital Communications*, 5th ed.; MacGraw-Hill: New York, NY, USA, 2007.
24. Xi, Y.; Burr, A.; Wei, J.B.; Grace, D. A general upper bound to evaluate packet error rate over quasi-static fading channels. *IEEE Trans. Wirel. Commun.* **2011**, *10*, 1373–1377. [CrossRef]

Disclaimer/Publisher's Note: The statements, opinions and data contained in all publications are solely those of the individual author(s) and contributor(s) and not of MDPI and/or the editor(s). MDPI and/or the editor(s) disclaim responsibility for any injury to people or property resulting from any ideas, methods, instructions or products referred to in the content.